

How Population III Supernovae Determined the Properties of the First Galaxies

KE-JUNG CHEN,¹ CHING-YAO TANG,^{1,2} DANIEL J. WHALEN,³ MENG-YUAN HO,^{1,2} SUNG-HAN TSAI,^{1,2} PO-SHENG OU,^{1,2} AND MASAOMI ONO^{1,4}¹*Institute of Astronomy and Astrophysics, Academia Sinica, Taipei 10617, Taiwan*²*Department of Physics, National Taiwan University, Taipei 10617, Taiwan*³*Institute of Cosmology and Gravitation, Portsmouth University, Portsmouth, UK*⁴*Astrophysical Big Bang Laboratory, RIKEN, Saitama 351-0198, Japan*

ABSTRACT

Massive Pop III stars can die as energetic supernovae that enrich the early universe with metals and determine the properties of the first galaxies. With masses of about $10^9 M_\odot$ at $z \gtrsim 10$, these galaxies are believed to be the ancestors of the Milky Way. This paper investigates the impact of Pop III supernova remnants (SNRs) from both Salpeter-like and top-heavy initial mass functions (IMFs) on the formation of first galaxies with high-resolution radiation-hydrodynamical simulations with the ENZO code. Our findings indicate that SNRs from a top-heavy Pop III IMF produce more metals, leading to more efficient gas cooling and earlier Pop II star formation in the first galaxies. From a few hundred to a few thousand Pop II stars can form in the central regions of these galaxies. These stars have metallicities of 10^{-3} to $10^{-2} Z_\odot$, greater than those of extremely metal-poor (EMP) stars. Their mass function follows a power-law distribution with $dN(M_*)/dM_* \propto M_*^\alpha$, where M_* is stellar mass and $\alpha = 2.66 - 5.83$ and is steeper for a top-heavy IMF. We thus find that EMP stars were not typical of most primitive galaxies.

Keywords: (cosmology:) early universe — galaxies: dwarf — galaxies: formation — hydrodynamics — methods: numerical — stars: Population III

1. INTRODUCTION

The birth of primordial (Pop III) stars at $z \sim 20 - 25$ marked the end of the cosmic dark ages and the onset of the first galaxy and supermassive black hole (SMBH) formation (Wise & Abel 2008a,b; Wise et al. 2012; Whalen & Fryer 2012; Smidt et al. 2018; Latif et al. 2021, 2022; Patrick et al. 2023). Pop III stars are thought to form in primordial mini halos that have grown to $10^5 - 10^6 M_\odot$ by mergers and accretion, when enough H₂ can form to cool gas and create stars. The original numerical simulations of Pop III star formation (SF) suggested that they have typical masses of $100 - 200 M_\odot$ and form in isolation, one per halo (Bromm et al. 2001; Nakamura & Umemura 2001; Abel et al. 2002), but later studies have since shown that they can form in binaries (Turk et al. 2009; Stacy & Bromm 2013) or small multiples (Stacy et al. 2010; Clark et al. 2011; Greif et al. 2011; Riaz et al. 2018; Susa 2019; Wollenberg et al. 2020; Sharda et al. 2020). The final mass of Pop III stars de-

pends on how many of them form in a halo, when their ionizing UV flux halts accretion (McKee & Tan 2008; Hosokawa et al. 2011; Susa 2013; Hirano et al. 2014, 2015), and whether or not they are ejected from the disk by gravitational torques (Greif et al. 2012). They have been found to range from less than a solar mass to up to several hundred solar masses. However, the Pop III IMF remains unknown because Pop III stars cannot be directly observed, and recent simulations included crucial physics such as magnetic fields and radiation transport cannot evolve to the main sequence at the required numerical resolution (Bromm et al. 2009; Glover 2013; Whalen 2013; Greif 2015; McKee et al. 2020; Stacy et al. 2022; Jaura et al. 2022).

Pop III stars radically transform their environments, first by photoevaporating the halos in which they are born (Whalen et al. 2004; Kitayama et al. 2004; Abel et al. 2007) and at least partially ionizing others nearby (Susa & Umemura 2006; Hasegawa et al. 2009). Then, depending on their masses, some explode as supernovae (SNe), expelling large masses of the first metals in the universe. Pop III stars with masses of $8 - 30 M_\odot$ die as

core-collapse (CC) SNe and $90 - 260 M_{\odot}$ stars explode as highly energetic pair-instability (PI) SNe (Heger & Woosley 2002, 2010). A few very rapidly-rotating $30 - 60 M_{\odot}$ Pop III stars may die as gamma-ray bursts (GRBs; e.g., Mesler et al. 2014) or hypernovae (HNe; e.g., Smidt et al. 2014; Chen et al. 2017b). A number of studies have examined how metals from Pop III SNe propagate into the universe on a variety of scales, from inside the halo itself (Sluder et al. 2016) to out into the relic H II region of the progenitor star (Greif et al. 2007; Ritter et al. 2012, 2016; Chen et al. 2017c; Magg et al. 2020; Tarumi et al. 2020; Latif & Schleicher 2020). Both radiation (Yoshida et al. 2007; Susa et al. 2009) and metals (Mackey et al. 2003; Schneider et al. 2006; Smith & Sigurdsson 2007; Smith et al. 2015) from the first stars cause subsequent generations of stars to form on smaller mass scales. Pop III SNe could constrain the masses of the first stars, either directly through their detection in the near-infrared (NIR; Tanaka et al. 2012, 2013; de Souza et al. 2013; Whalen et al. 2013a,b,c,d; de Souza et al. 2014; Hartwig et al. 2018a; Moriya et al. 2019; Rydberg et al. 2020) or indirectly from their nucleosynthetic imprint on less massive second-generation stars that may still live today (e.g., Frebel et al. 2005; Beers & Christlieb 2005; Iwamoto et al. 2005; Joggerst et al. 2010; Frebel 2010; Joggerst & Whalen 2011; Susa et al. 2014; Chen et al. 2017a,c; Ishigaki et al. 2018; Hartwig et al. 2018b, 2019; Chiaki et al. 2018; Chiaki & Tomi-naga 2020).

When the halos grow to $10^8 - 10^9 M_{\odot}$ through hierarchical structure formation by mergers and accretion, they are massive enough to maintain consecutive cycles of stellar birth and explosion without all the fuel for forming new stars being blown into the IGM, becoming, in effect, the first galaxies (Greif et al. 2008; Bromm & Yoshida 2011). Unlike other low-mass dwarf galaxies across cosmic time, the baryon components of these first galaxies were primordial gas and Pop III SNRs. Ionizing photons, winds, and SNe from stars in these galaxies regulate the rise of later generations and determine their observational signatures (Greif et al. 2010; Jeon et al. 2012; Pawlik et al. 2013; Wise et al. 2012; Safranek-Shrader et al. 2014; Jeon et al. 2014; Corlies et al. 2018; Jeon & Bromm 2019; Abe et al. 2021). The simulations of first galaxies performed to date follow their formation in cosmological environments from early times but assume a fixed IMF for Pop III and Pop II stars that does not evolve over time (e.g., O’Shea et al. 2015; Paardekooper et al. 2015).

To probe the Pop III IMF, we take Pop III SNRs from two IMFs, Salpeter-like (Salpeter 1955) and Hirano (Hirano et al. 2015) as an initial condition and simulate the

evolution of SNRs with the primordial gas until the first galaxies form. Our goal is to understand how the properties of the first galaxies vary with the properties of Pop III SNRs that depend on the Pop III IMF. The observational signatures of these galaxies may be revealed by the *James Webb Space Telescope* (JWST; Gardner et al. 2006; Kalirai 2018) and 30 – 40 m telescopes on the ground in the coming decade.

The structure of this paper is as follows. In Section 2, we describe our numerical methods and protogalaxy models. We present the simulations of the collapsing Pop III SNRs in the proto-galaxy in Section 3, and the resulting Pop II SF in Section 4. Finally, we discuss the limits of our simulations in Section 6 and conclude in Section 7.

2. NUMERICAL METHOD

We model the formation of first galaxies with the ENZO adaptive mesh refinement (AMR) cosmology code (v2.5; Bryan et al. 2014). ENZO uses an adaptive particle-mesh N -body scheme (Efstathiou et al. 1985; Couchman 1991) to evolve dark matter (DM) and a third-order accurate piecewise-parabolic method for gas flow (Woodward & Colella 1984; Bryan et al. 1995). We use the low-viscosity Harten-Lax-van Leer-Contact (HLLC) Riemann method (Toro et al. 1994) for capturing strong shocks and rarefaction waves to prevent negative energies or densities in the simulation. ENZO self-consistently evolves nine-species non-equilibrium gas chemistry with hydrodynamics (H , H^+ , e^- , He , He^+ , He^{++} , H^- , H_2 and H_2^+ ; Abel et al. 1997; Anninos et al. 1997) and includes primordial gas cooling in the energy equation: collisional excitational and ionizational cooling by H and He , recombinational cooling, bremsstrahlung cooling and H_2 cooling. We use H_2 cooling rates from Glover & Abel (2008) and metal cooling rates from Glover & Jappsen (2007).

2.1. Protogalaxy Model

The protogalaxies in our simulations are approximated as isolated Navarro-Frenk-White (NFW) halos (Navarro et al. 1996) whose DM density profiles are

$$\rho_{\text{DM}}(r) = \frac{\rho_0}{\frac{r}{R_s}(1 + \frac{r}{R_s})^2}, \quad (1)$$

where r is the radius and ρ_0 and the "scale radius" R_s depend on the physical properties of the halo. This profile is used to initialize the gravitational potential of the DM in the halo but DM dynamics itself is not included in our runs so this potential held fixed over the run. We adopt idealized profiles for the initial structure of the protogalaxy instead of evolving them from

primordial density fluctuations at high redshifts so we can efficiently run models and examine the impact of Pop III SN remnants (SNRs) on their structures at later times. Because the DM halos for first galaxies formed at $z \sim 10 - 15$, these halos have a more compact structure than our present-day galaxies. For our simulations, we use the scale radius of 1000 pc for a non-rotating $10^9 M_\odot$ DM halo, with a total gas mass of $M_g \sim 1 \times 10^8 M_\odot$ for our protogalaxy.

DM in the first galaxies is composed of swarms of DM minihalos that have gravitationally congregated into a more massive bound structure, not the smooth NFW profiles with which we initialized our models. Most of the mass in the galaxy is in the form of these smaller halos. Our simulations therefore do not properly account for their point-mass contribution to the true potential in the halo. The immediate consequence of this for our models is that they underestimate mixing of metals from SNRs in the interior of the halo. Tidal torquing between constituent minihalos in the galaxy would eject streams of gas from their SNRs and promote mixing of their metals with ambient pristine gas.

Pop III SNRs are initialized from Pop III SNe in cosmological environments in [Chen et al. \(2014, 2015\)](#), as shown in Figure 1. Depending on the SN type, Pop III SNRs can reach radii of $0.5 - 2$ kpc with metallicities of $\sim 10^{-4} - 10^{-2} Z_\odot$. By assuming spherical symmetry and neglecting the clumpy structures, we calculate 1D simplified profiles of density, temperature, and metallicity of Pop III SNRs based on [Chen et al. \(2015\)](#) and show these profiles in Figure 2 and initialize these profiles as the pre-existing SNRs at the beginning of each run. Based on [Chen et al. \(2015\)](#), these profiles consider the relic H II region of the star, which can expand the size of SNRs after it comes into pressure equilibrium in the warm, partially recombined gas ([Greif et al. 2007](#)). Our SNRs are produced by three types of SN explosions: a $15 M_\odot$ CC SN (1.2 foe), a $60 M_\odot$ HN (10 foe), and a $250 M_\odot$ PI SN (100 foe), where $1 \text{ foe} = 10^{51} \text{ erg}$. The metal yields of these explosions are $1.8 M_\odot$, $26.4 M_\odot$, and $109 M_\odot$, respectively. The SNRs are randomly distributed throughout the halo but are all assigned free-fall velocities towards its center.

Because we do not evolve halos in cosmological environments, we ignore temperature floors in the gas imposed by the cosmic microwave background (CMB). The CMB can affect the mass scales of fragmentation in gas in minihalos at early times. However, at the typical redshifts of formation of first galaxies the CMB floor is $30 - 45$ K, similar to the temperatures to which metals and dust can cool gas at the low metallicities in our models. Exclusion of the CMB will therefore have negligible

effects on the mass scales of star formation in our simulations.

Our $10^9 M_\odot$ DM halo is composed of hundreds of minihalos but only a few tens of them were originally massive enough to host Pop III stars or SNRs. The initial numbers and types of SNRs in the massive halo are determined by the choice of Pop III IMF. Here, we consider a Salpeter-like IMF (SAL; [Salpeter 1955](#); [Kroupa 2001](#); [Chabrier 2003](#)) with a peak at $10 M_\odot$ and a top-heavy IMF from [Hirano et al. \(2015\)](#) (HIR15). We assume a Salpeter IMF with a peak at $10 M_\odot$ for massive stars because it is the approximate lower limit in progenitor mass for CC SNe. A number of recent studies also suggest that Pop III stars may have had typical masses of a few tens of solar masses ([Hasegawa et al. 2009](#); [Hosokawa et al. 2011](#); [Hirano et al. 2014, 2015](#); [Latif et al. 2022](#)).

If we use the SAL IMF, 18 CC SNe and 2 HNe are initialized in the halo. In the case of the HIR15 IMF, the halo contains 2 CC SNe and 7 PI SNe. We randomly distribute these SNRs throughout the halo. Gas densities in our halos marginally trace the NFW DM profiles because the gas is assumed to have already settled in the gravitational potential to some degree by the time we begin to evolve them. We consider two gas density profiles of $\rho(r) \sim r^{-1}$ and $\rho(r) \sim r^0$ in the halo to examine the effect of gas distribution formed during the assembly of mini halos. Furthermore, all density profiles are non-hydrostatic equilibrium.

The halo is centered in a 10 kpc box with a 128^3 root grid with outflow boundary conditions. To resolve the structure of SNRs, we use up to 10 levels of AMR. The grid is flagged for refinement where the gas overdensity is $8\rho_0 N^l$, where $\rho_0 = 1.673 \times 10^{-27} \text{ g cm}^{-3}$ is the ambient density of the halo, $N = 8$ is the refinement factor, and l is the AMR level of the grid patch. In the densest regions, this procedure yields a maximum spatial resolution of 0.077 pc, which is sufficient to resolve the shell mergers between SNRs, and the central SF sites at later times.

2.2. Star Formation

Our galaxy simulations have a spatial resolution of up to 0.077 pc, which is high enough to resolve metal mixing and star-forming clouds in the halo at later times but not Pop II SF. In the high density region, each cell mass represents a small patch of the molecular cloud that later forms a single star. We adopt a subgrid model of SF from [Cen & Ostriker \(1992\)](#) and assume a Pop II SF efficiency $\epsilon_{\text{SF}} = 0.05$, in which 5% of the mass of the gas in a cell that satisfies the criteria for SF is converted into a star particle. This conversion efficiency is moti-

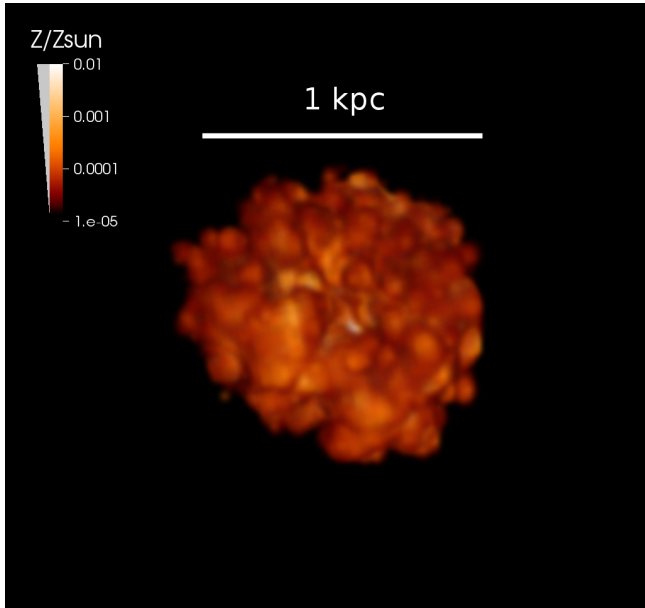


Figure 1. Metallicity distribution of a Pop III SNR. This iso-surface plot shows the morphology of a HN SNR of a $60 M_{\odot}$ Pop III star 10 Myr after the explosion. The SNR has expanded to a radius of 1 kpc and enriched the surrounding gas to metallicities of $\sim 10^{-4} - 10^{-2} Z_{\odot}$ (Chen et al. 2015).

vated by studies of SF in the local universe that suggest that only a small fraction of molecular gas is converted into stars (Evans et al. 2009; Krumholz et al. 2019; Kim et al. 2021). In reality, it may vary depending on the resolution of the simulations and the physical conditions in SF regions. Since cloud structure is marginally resolved in our simulation, the SF efficiency here represents a lower limit. SF cells in our simulations normally contain $\sim 20 - 500 M_{\odot}$ of gas, which leads to typical masses of several to tens of solar masses for Pop II stars.

2.3. Stellar Feedback

After star particles form in the simulations, their radiation feedback to surroundings is on during their lifetime. We model the feedback of ionizing UV photons from massive stars with the MORAY ray-tracing package (Wise & Abel 2011). MORAY includes radiation pressure on gas due to photoionization and the radiation is self-consistently coupled to gas hydrodynamics, cooling, and chemistry in ENZO. Each star particle is treated as a point source that emits both ionizing and Lyman-Werner (LW) photons. The luminosities and lifetimes for new-born Pop III stars¹ formed during the simula-

tions use the table from Schaerer (2002). For individual Pop II stars, we have calculated their luminosity function using 1D stellar evolution models with MESA (Paxton et al. 2011, 2013, 2015, 2018).

Stellar winds may reshape the ambient media of massive stars and affect the dynamical evolution of SNRs (Dwarkadas 2005). However, we neglect the feedback of stellar winds from Pop III stars because the zero metallicity suppresses the stellar wind significantly. On the other hand, stellar wind of Pop II stars vary as $\dot{M} \propto Z^m$ where $m \sim 0.1 - 1$ for metallicities down to $0.01 Z_{\odot}$ (Vink et al. 2001; Smith 2014). Since the Pop II stars in the first galaxies likely form with metallicities of $Z < 0.01 Z_{\odot}$, the winds for these low-metallicity stars are weak and uncertain (Ou et al. 2023). Therefore, we also exclude the wind feedback of Pop II stars in our runs.

Some of the massive Pop II and Pop III stars eventually die as SNe at the end of their life and produce strong feedback to their surroundings. Explosion energy from Pop II and Pop III SNe is deposited in the gas as thermal energy rather than linear momentum (e.g., Whalen et al. 2008b). This practice in principle can lead to the classic overcooling problem, in which large amounts of thermal energy deposited in high densities are radiated away by cooling before they can create the large pressure gradients that drive shocks outward, as in real explosions. However, this issue is resolved in our runs because our high resolution allows us to follow radiative cooling accurately. Furthermore, as discussed in the Introduction 1, ionizing UV flux from the star drives gas from it in strong supersonic flows and the explosions always occur in low densities (stellar winds have a similar effect when present; Chen et al. 2015; Smidt et al. 2018). Consequently, sound-crossing times in our models are shorter than cooling times and SNe can drive strong shocks in our runs.

We performed eight runs in which we used the initial SNRs based on two Pop III IMFs, and two mass scales of the Pop III stars that form during the run, and two gas density profiles for the halo. These models are divided into four groups, and what varies between models in a group is the mass scale of Pop III stars that form in them. The model parameters are summarized in Table 1. SF rates in the galaxies in our models level off as ionizing UV, and SNe due to stars begin to suppress the formation of new stars. Since we are mostly interested in the transition from Pop III to Pop II SF (and computational costs rise as more stars form), the simulations are evolved for 35 – 60 Myr when SF flattens out and the properties of the stellar populations in the nascent galaxies stabilize.

¹ These newborn Pop III stars known as Pop III.2 (Hirano et al. 2015) might have experienced the radiative feedback from earlier Pop III stars. Since we do not include the radiative feedback from these Pop III stars, we treat the Pop III.2 stars as Pop III stars.

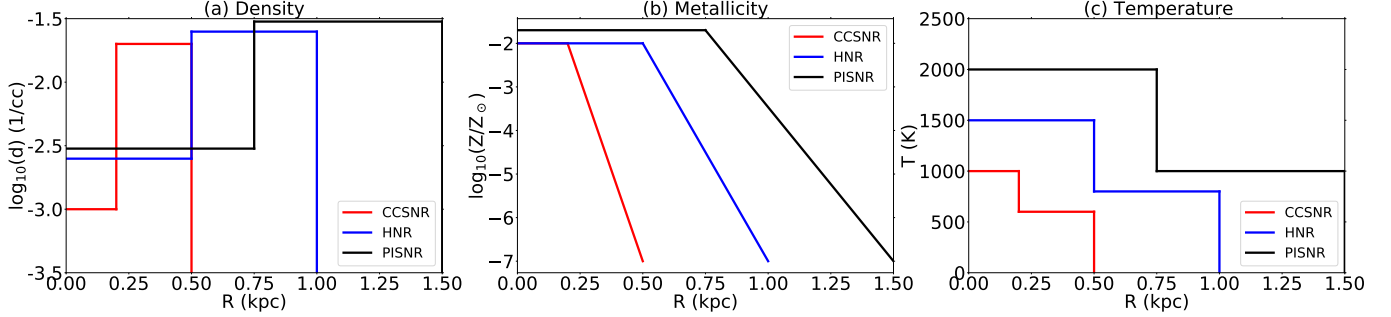


Figure 2. Left to right: radial profiles of number density, metallicity, and temperature of the three types of SNRs in our simulations, respectively.

Model	M_{halo}	SNR IMF	$\rho(r)$	M_{PopIII}	N_{CC}	N_{HN}	N_{PI}
A1	10^9	SAL	$r^{-1.0}$	20	18	2	0
A2	10^9	SAL	$r^{-1.0}$	200	18	2	0
B1	10^9	HIR15	$r^{-1.0}$	20	2	0	7
B2	10^9	HIR15	$r^{-1.0}$	200	2	0	7
C1	10^9	SAL	r^0	20	18	2	0
C2	10^9	SAL	r^0	200	18	2	0
D1	10^9	HIR15	r^0	20	2	0	7
D2	10^9	HIR15	r^0	200	2	0	7

Table 1. Model parameters. Left to right: model, halo mass (M_{\odot}), Pop III SNR IMF, baryon density profile, Pop III star mass (M_{\odot}), number of CC SNRs, number of HN SNRs, and number of PI SNRs.

3. ACCRETION OF POPULATION III SUPERNOVAE REMNANTS

3.1. Collapse of Pop III SNRs

The in-falling time for the outermost SNRs to reach the halo center is about $30 - 40$ Myr. Since the gravity of the halo is dominated by the dark matter, the in-falling time for most of gas to reach the center is similar among models. We first show the density evolution of simulations in Figure 3. At $t = 0$, the range of filling factors of SNRs is due to the energy of SN explosions: larger PI SNRs in B1 and D1 are easily distinguished from the less energetic CC SNRs in the A1 and C1 runs. These Pop III SNRs and the primordial gas are dragged by the halo gravity toward its center. Meanwhile, the SNR-SNR collisions produce a range of turbulent flows at the center, from fairly violent ones in the B and D models. Eventually, the turbulence drives the mixing of SNR metal and primordial gas and creates filamentary structures that soon form into dense clumps due to the self-gravity and metal cooling of the gas.

3.2. Feedback from New Population III Supernovae

Before the initial SNRs accrete, the primordial gas has been accumulated at the halo center and formed Pop III stars, which compositions remain primordial but

experience the UV radiation from earlier Pop III stars. These Pop III stars only form in the A and B runs with a steeper gas density profile of r^{-1} . For C and D runs, the pre-existing SNRs around the halo center prevent the consequent Pop III SF.

These massive Pop III stars can impose strong radiative and SN feedback before the initial Pop III SNRs reach the halo center. We show radiative feedback and metal injection of a Pop III star in Figure 4. This Pop III star of $200 M_{\odot}$ heats and ionizes surrounding gas, which can either suppress or promote new SF in its vicinity (Whalen et al. 2008a, 2010). After its short lifetime of ~ 2.0 Myr, the star dies as a PI SN and its shock heats the gas to high temperatures ($> 10^5$ K) and ejects a large mass of metals that enhance cooling and promotes a transition to Pop II SF. The existence of Pop III stars in the first galaxies is promising, but due to a rapid pollution of metals from Pop III SNRs; only a small fraction of pristine gas could form Pop III stars. Therefore, Pop III stars cannot be the major components of the first galaxies. Only one or two Pop III stars could form in A and B models; their metal contributions to the halo is small in compared to that of the initial Pop III SNRs. However, most of Pop III stars form around the halo center that also hosts the later Pop II SF. Therefore, the stellar and SN feedback of Pop III stars may still affect the Pop II SF in the first galaxies.

3.3. Chemical Enrichment

To examine the chemical enrichment by Pop III SNRs, we first show the metallicity distribution for A1 - D1 model in the left panel of Figure 5, before the Pop II SF. The accretion of PI SNRs in the HIR15 IMF cases (B1 and D1) results in much concentrated and high metallicity regions than in SAL IMF cases (A1 and C1). Despite some SNRs are still approaching to the halo center, the central metallicity of $r < 200$ pc is enriched by both the new Pop III SNRs and the original Pop III SNRs. We find that halos with Pop III PI SN remnants in B1 and D1 exhibit stronger turbulent mixing in their densest re-

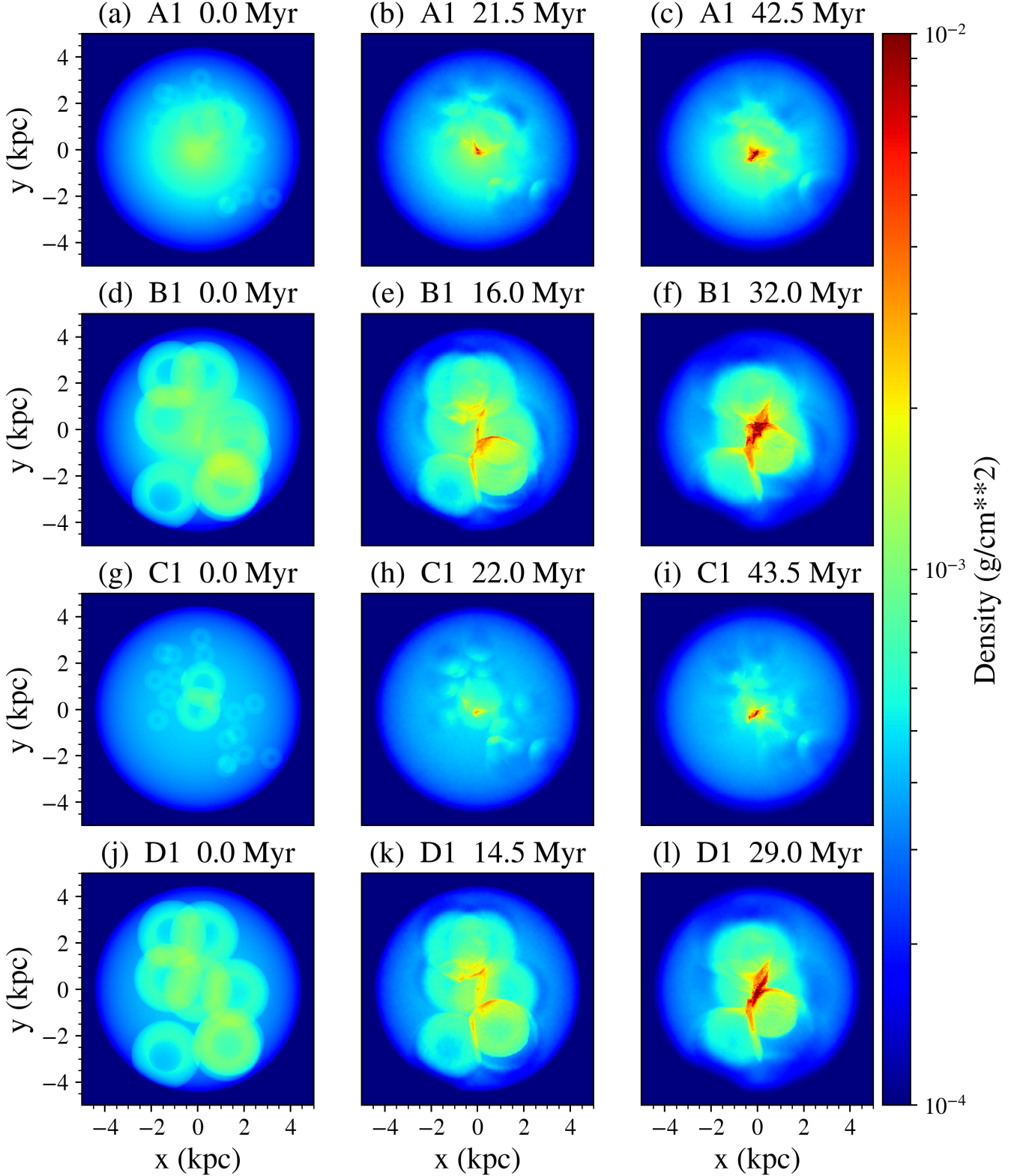


Figure 3. Density distribution at the beginning, intermediate, and final stages of the A1, B1, C1, and D1 runs before the Pop II SF. Collisions of Pop III SNRs create filamentary structures and drive the mixing between the metals and primordial gas. The mixed gas eventually collapses to the halo center, where SF would occur shortly.

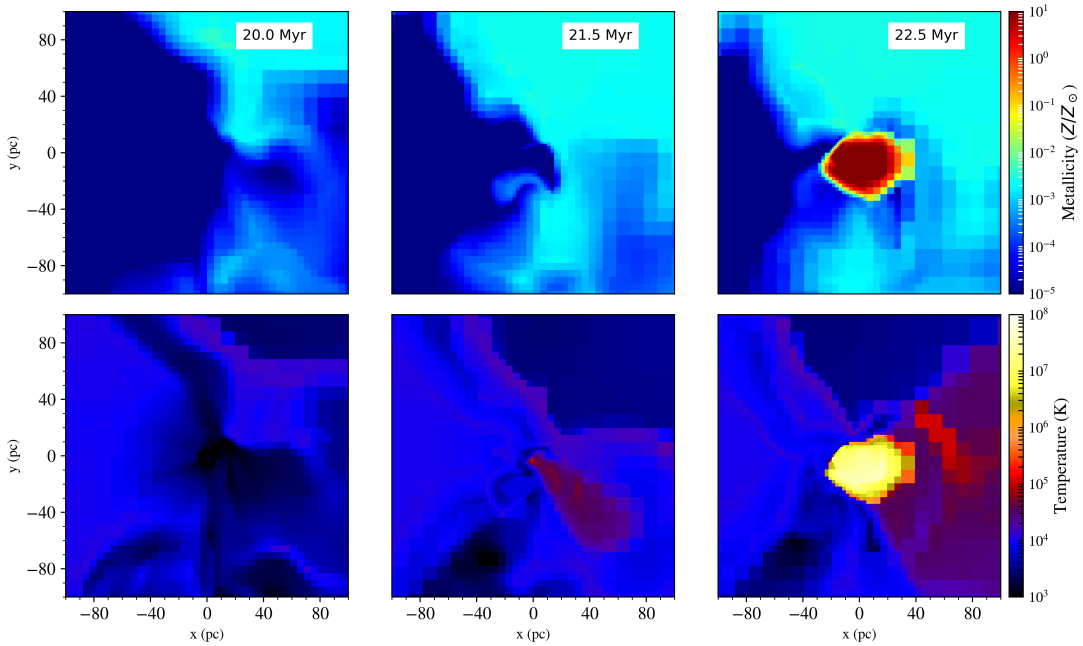


Figure 4. Metallicity and temperature slices of the central 200 pc, where a $200 M_{\odot}$ Pop III star forms in A2. Left to right: 20 Myr (right before birth), 21.5 Myr (1.5 Myr after birth), and 22.5 (0.5 Myr after death). After the star born, its radiation heats and ionizes the surrounding gas and creates a giant HII region as shown in the middle panel. When the star dies as a PI SN, the explosion forms a new SNR of hot and metal-rich ejecta visible in the right panels.

gions by showing a uniform metallicity across the inner region, because the remnants collide with greater energy when they reach the halo center. In fact, the yields of Pop III CCSNe, HNe, and PISNe produce unique abundance patterns that can leave fingerprints on the Pop II stars for decoding the nature of Pop III stars. Tracing each individual element from each SN requires a huge advection network that is computationally expensive. Therefore, we do not trace the individual elements in our simulations but only consider the total amount of metal by summing all elements of SN yields.

We show spherically-averaged profiles of metallicities for the A1 - D1 runs before the Pop II SF in Figure 5. The metallicity in all models ranges from $2 \times 10^{-4} - 5 \times 10^{-3} Z_{\odot}$. The metallicity rises in the inner region of A1 is due to the chemical enrichment of Pop III stars and the rise in C1 is due to an initialed SNR at the center. Finally, we show the density, temperature, and metallicity phase diagram in the left panel of Figure 6. Maximum densities of the gas clumps can reach above 10^5 cm^{-3} with metallicities of $Z \geq 10^{-3}$ at temperatures of $10 - 100 \text{ K}$. As time evolves, these dense gas clumps eventually collapse and give birth to the Pop II stars.

4. POP II STAR FORMATION IN THE PROTOGALAXY

The accreting Pop III SNRs and the primordial gas eventually trigger the Pop II SF around the halo center at $30 - 35 \text{ Myr}$ when the dense clumps satisfy the SF criteria. Due to the effective metal cooling, the mass scale of these Pop II stars shifted to a low mass-end and formed in a cluster as shown in the right panel of Figure 6. In our simulations, the metal cooling acts on the cloud scale, and the inhomogeneous mixing of metal drives the fragmentation of clouds, forming into SF clumps. We exclude the effect of SF disk fragmentation (Clark et al. 2011; Chiaki et al. 2018; Sharda et al. 2020) due to metal and dust cooling in the sub-grid scale. Several star-forming regions appear in our simulations due to the inhomogeneous mixing of SNRs and primordial gas. The SF mainly locates along the filaments of dense structures within the central 200 pc of the halo. Most stars form within a few million years until their stellar feedback disrupts the star-forming could and prevents further SF. The Pop II SF begins later in SAL halos than in HIR15 halos because a weaker metal cooling delays the SF. Among all models, about $170 - 2,295$ Pop II stars form in this episode of SF and produce total stellar mass $\sim 225 - 3,966 M_{\odot}$ (see Table 2 for details).

4.1. The Mass Function

We show the mass functions of Pop II stars in Figure 7. Most of the mass functions can be fitted using a

power-law distribution, $dN_*/dM_* \propto M_*^{-\alpha}$, where N_* is the number of stars and M_* is the mass of the stars. The most massive Pop II star in our simulations is $\sim 13.6 M_{\odot}$ in A2. In C and D models, the mass function becomes slightly irregular, with a second peak appearing at the high mass end. In these cases, low-mass stars formed first, creating the first peak. Then radiative feedback from these Pop II stars heated the surrounding clouds and increased their Jeans masses, that led to more massive star formation shown as the second peaks in Figures 7. These mass functions could place constraints on the Pop III SNRs if the power-law indices of the stellar mass functions of our model galaxies hold until their Pop II SF becomes a steady state.

We find that power-law index, α varies from $2.66 - 5.83$ across all eight models and this value is higher than $2.3, \alpha$ of the Salpeter IMF (Salpeter 1955; Kroupa 2001; Chabrier 2003). Comparing all models, we find that the models seeded with PI SNRs results have larger α and steeper slopes in the power-law for the mass functions. Before Pop II SF, stronger metal cooling and turbulence driven by PI SNRs can fragment enriched clouds and decrease the mass scale of Pop II stars and result in steeper slopes. The change in IMF slope can be understood by considering the Jeans mass of the clouds,

$$M_j \approx 13.7 M_{\odot} \left(\frac{T}{50 \text{ K}} \right)^{3/2} \left(\frac{\rho}{10^{-20} \text{ g cm}^{-3}} \right)^{-1/2}, \quad (2)$$

where ρ is gas density and T is the temperature. The Jeans mass is more sensitive to changes in temperature than density. As shown in the phase diagram in Figure 6, the Jeans mass varies from $1.22 - 38.7 M_{\odot}$ for temperatures of $10 - 100 \text{ K}$ at densities of $10^{-20} \text{ g cm}^{-3}$. The cell masses are 20 to $500 M_{\odot}$, indicating that the majority of them are poised for imminent collapse and star formation. In Figure 6, gas temperatures at $\rho \sim 10^{-20} - 10^{-18} \text{ g cm}^{-3}$ are generally lower in B1 than in A1 because B1 has a higher metallicity. Enrichment by PI SNRs can create higher metallicities and stronger turbulence, facilitating the mixing of metals toward the center of the halo where star formation occurs. The higher metallicities cool gas to lower temperatures and result in smaller Jeans masses, promoting low-mass star formation and the steepening the IMF slope.

4.2. Stellar Metallicity

We now examine the stellar metallicity of Pop II stars by exhibiting their metallicity distributions in Figure 8. Stars in A2 and B2 runs have the highest metallicities because new Pop III stars die as PI SNe and inject the most metals into the halo center. Overall, the B and D models have higher metallicities than the A and C

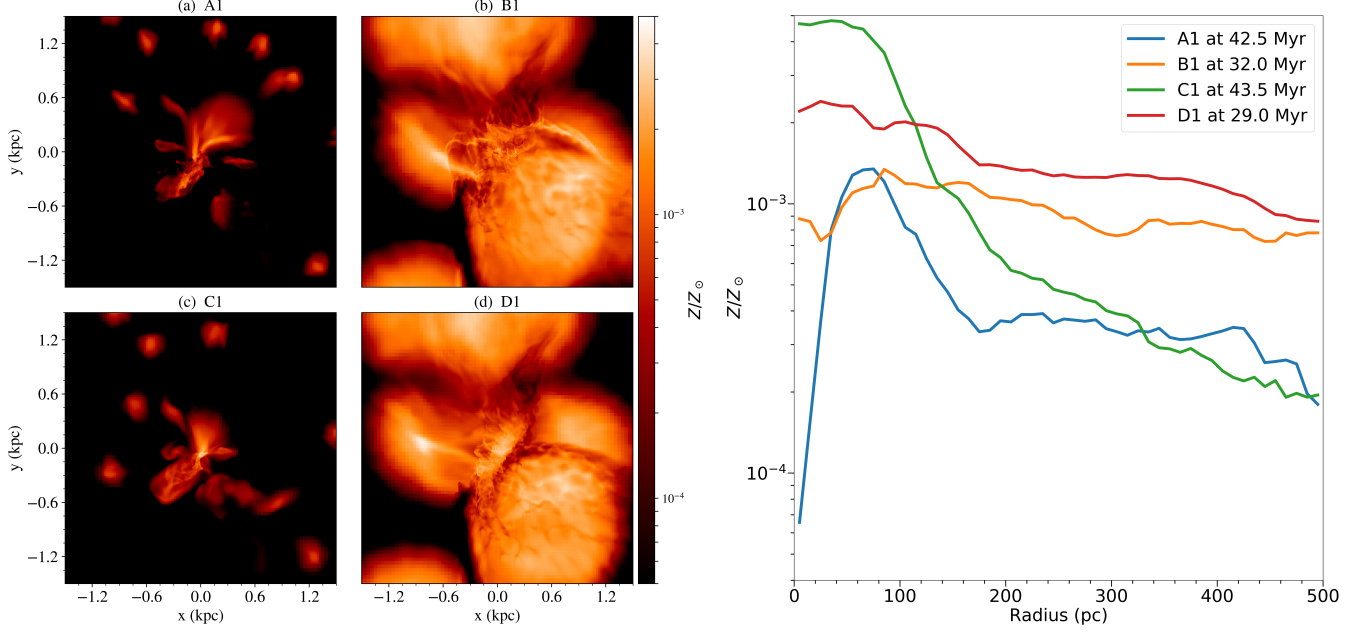


Figure 5. Left: Metallicity distribution before the Pop II SF at A1, B1, C1, and D1 runs. Panels show slices of metallicity at the central 3.0 kpc region, where metals of the Pop III SNRs have reached the centers and chemically enriched the primordial gas to metallicity of $10^{-4} - 10^{-3} Z_{\odot}$ at large. Right: The corresponding 1D spherically-averaged metallicity profiles of $r < 500$ pc.

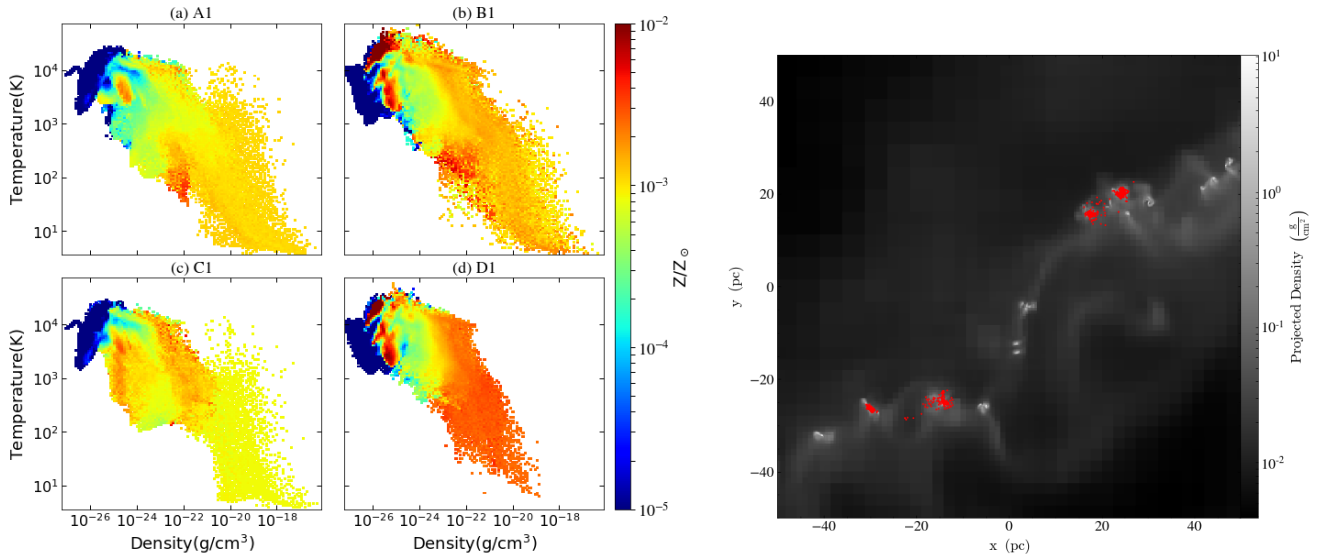


Figure 6. Left: The phase diagram of densities, temperatures, and metallicities of the gas inside the first galaxy before the Pop II SF. The star-forming gas is located at the high-density and low-temperature region as shown in the bottom-right corner in each panel. The gas temperatures and densities are also associated with its metallicity. The Pop II SF region in B1 and D1 contains higher metallicity than that in A1 and C1. Some high-density regions have been cooled down to ~ 10 K because we ignore the ambient gas temperatures heated by the cosmic background radiation. Right: The Pop II SF regions in A1. Red dots represent individual Pop II stars. Due to the metal cooling and turbulence, these Pop II stars form into clusters along the dense filaments around the halo center.

Model	t_{evol} (Myr)	N_{PopII}	M_* (M_\odot)	N_{PopIII}	α	L (L_\odot)
A1	45.5	1742	3350	2	2.81	3.23×10^5
A2	37.0	2022	3966	1	2.82	6.00×10^5
B1	32.5	1949	2387	1	5.83	1.39×10^4
B2	33.5	1968	2655	1	4.58	2.76×10^4
C1	58.0	170	225	0	2.66	1.92×10^3
C2	53.5	234	391	0	2.78	8.57×10^3
D1	32.5	2295	3409	0	4.18	5.57×10^4
D2	37.5	1241	1692	0	4.38	1.77×10^4

Table 2. Summary of stellar populations in all models. Left to right: model name, evolution time, the final number of Pop II stars, total stellar mass, number of Pop III stars formed during the simulation, α (the power-law index of mass function, $dN_*/dM_* \propto M_*^{-\alpha}$), and total luminosity.

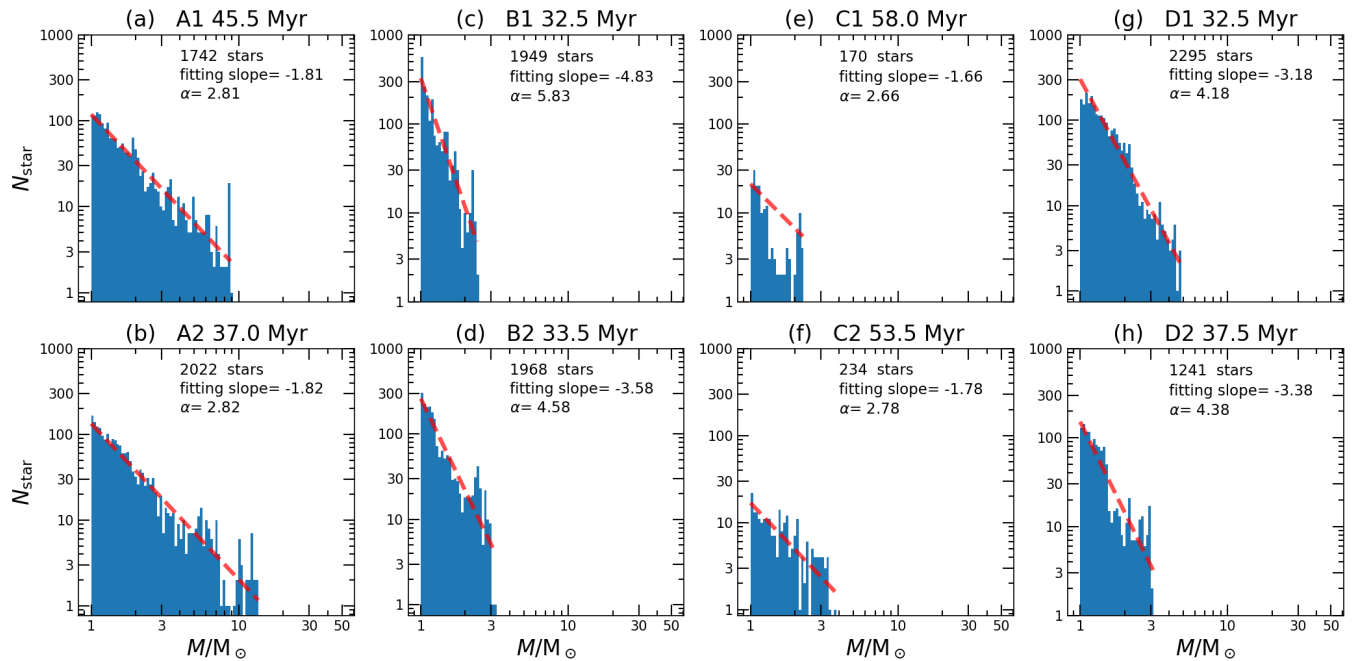


Figure 7. The Pop II mass function in first galaxies. No Pop III stars remain at the end of any of the runs. The mass function can be fitted with a power-law function in most runs. The total number of stars, the best-fit index α , and the fitting line slope $1 - \alpha$ are listed in each panel.

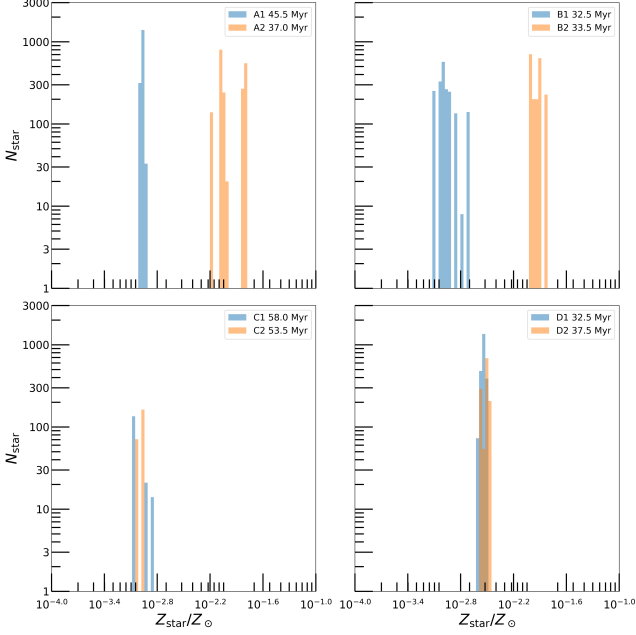


Figure 8. Metallicity distribution of the Pop II stars in first galaxies. Each model has a stellar population within a metallicity range of $10^{-3} - 2 \times 10^{-2} Z_{\odot}$. Because only A and B models form the Pop III stars, they create a more dispersed stellar metallicity distribution between A1 and A2, and B1 and B2 due to the metals from the Pop III SNe.

models because of the initial PI SNRs. The metallicity distribution of the C and D series is more confined than the A or B series because no Pop III stars form to further enrich the gas. Small variations in metallicity within C and D series are due to the variations in the initial distributions of SNRs. The gas at the center of the halo in the D series is more turbulently mixed by collisions between PI SNRs there (as seen in the (d) panel in Figure 5). Therefore, there is even less variation in metallicity than in the D series.

4.3. Stellar Dynamics

Newly born Pop II stars can inherit a drift velocity from the motion of their star-forming cloud. If this velocity exceeds the escape velocity of a halo, stars will escape the halo without contributing to its luminosity. We examine this probability of runaway Pop II stars by showing the final Pop II star velocity distributions in Figure 9. Pop II stars have velocities of $< 30 \text{ km s}^{-1}$, but the escape velocity of a $10^9 M_{\odot}$ halo is $\sim 45 \text{ km s}^{-1}$ in A - D. Therefore, all Pop II stars will remain in their host halo.

4.4. Correlating the Pop III IMF with the First Galaxies

Most Pop II stars in the first galaxies form with $Z \geq 10^{-3} Z_{\odot}$, exceeding the metallicity of extremely metal-poor (EMP) stars, $Z \sim 10^{-5} - 10^{-4} Z_{\odot}$ (Umeda & Nomoto 2002; Frebel 2010). Consequently, EMP stars are not representative of Pop II stars in the earliest galaxies. Their mass function follows a power law whose indices depend on SNR type and the Pop III IMF. Top-heavy Pop III IMFs (Hirano et al. 2015, 2017) create metal-rich PI SNRs that enhance metal cooling and eventually lead to steeper slopes for the early Pop II IMF, less massive Pop II stars, and dimmer galaxies at early times than Salpeter Pop III IMFs.

5. CONCLUSION

We have investigated how Pop III SNRs bridge the death of the first stars and the rise of the first galaxies with high-resolution simulations. We find that they rapidly enriched gas in massive halos with metals and drove turbulence as they gravitated toward the centers of the halos. Subsequent populations of stars appeared at earlier times in these galaxies if the Pop III IMF was top-heavy because the gas in halos became contaminated by metals more quickly, cooling and forming stars. This trend is primarily due to PI SNe producing nearly 100 times the metals of CC SNe and more than 10 times the metals of HNe (Heger & Woosley 2002, 2010).

PI SNe in our protogalaxies consistently enrich star-forming gas to metallicities of $10^{-3} - 10^{-2} Z_{\odot}$, above those targeted by most surveys of EMP stars to date (e.g., Cayrel et al. 2004; Beers & Christlieb 2005; Aoki et al. 2014; Placco et al. 2016). This likely accounts for their failure to conclusively identify the 'odd-even' nucleosynthetic fingerprint of these explosions (Heger & Woosley 2002; Karlsson et al. 2008). Indeed, in the first confirmed detection of the odd-even effect in a metal-poor star, LAMOST J1010+2358 (Xing et al. 2023), happened at a metallicity of $[\text{Fe}/\text{H}] = -2.4$, consistent with those of the galaxies in our models with PI SNRs.

Our simulations also indicate that Pop III stars were not a major component of most early galaxies because gas in massive halos was usually polluted by metals from other Pop III SNe during hierarchical assembly before it could collapse into pristine stars. In future work, we will evolve our galaxies to larger masses to better determine the evolution of the mass function of Pop II stars over time. Followups to the *JWST* CEERS and JADES surveys in coming years will achieve greater depths and probe the properties of the first galaxies and second generation stars in the coming decade.

Acknowledgements

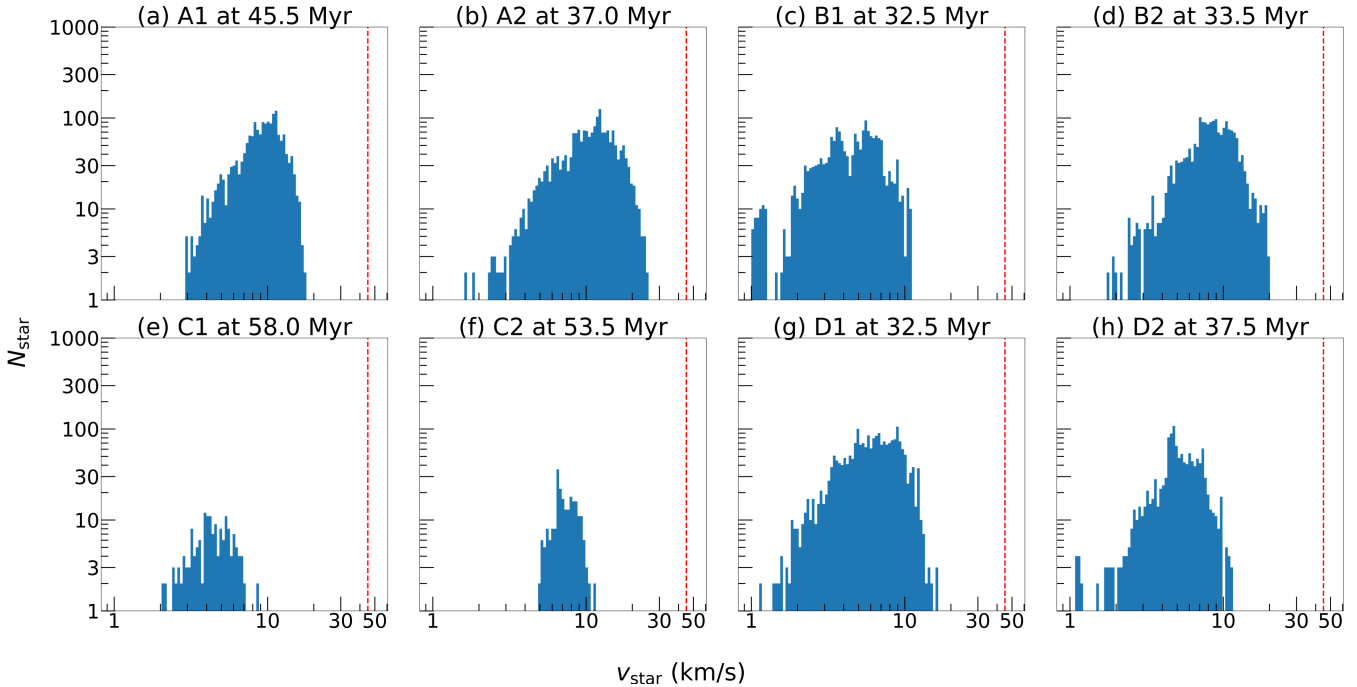


Figure 9. Stellar velocity distributions at the end of each run. In all models, the drift velocities of Pop II stars are below the escape velocity of halos of $\sim 45 \text{ km s}^{-1}$ denoted with red lines.

The authors thank Li-Hsin Chen for her support with the ENZO simulations and analysis. We also thank Hiroyuki Hirashita and You-Hua Chu for useful comments. K. C. was supported by the National Science and Technology Council, Taiwan under grant no. MOST 110-2112-M-001-068-MY3 and the Academia Sinica, Taiwan under a career development award under grant no. AS-CDA-111-M04. Numerical simulations were performed

at the National Energy Research Scientific Computing Center (NERSC), a U.S. Department of Energy Office of Science User Facility operated under Contract No. DE-AC02-05CH11231, at the Center for Computational Astrophysics (CfCA) at the National Astronomical Observatory of Japan (NAOJ), and at the TIARA Cluster at the Academia Sinica Institute of Astronomy and Astrophysics (ASIAA).

REFERENCES

Abe, M., Yajima, H., Khochfar, S., Dalla Vecchia, C., & Omukai, K. 2021, MNRAS, 508, 3226

Abel, T., Anninos, P., Zhang, Y., & Norman, M. L. 1997, New Astronomy, 2, 181

Abel, T., Bryan, G. L., & Norman, M. L. 2002, Science, 295, 93

Abel, T., Wise, J. H., & Bryan, G. L. 2007, ApJL, 659, L87

Anninos, P., Zhang, Y., Abel, T., & Norman, M. L. 1997, New Astronomy, 2, 209

Aoki, W., Tominaga, N., Beers, T. C., Honda, S., & Lee, Y. S. 2014, Science, 345, 912

Beers, T. C., & Christlieb, N. 2005, ARA&A, 43, 531

Bromm, V., Ferrara, A., Coppi, P. S., & Larson, R. B. 2001, MNRAS, 328, 969

Bromm, V., & Yoshida, N. 2011, ARA&A, 49, 373

Bromm, V., Yoshida, N., Hernquist, L., & McKee, C. F. 2009, Nature, 459, 49

Bryan, G. L., Norman, M. L., Stone, J. M., Cen, R., & Ostriker, J. P. 1995, Computer Physics Communications, 89, 149

Bryan, G. L., Norman, M. L., O'Shea, B. W., et al. 2014, ApJS, 211, 19

Cayrel, R., Depagne, E., Spite, M., et al. 2004, A&A, 416, 1117

Cen, R., & Ostriker, J. P. 1992, ApJL, 399, L113

Chabrier, G. 2003, PASP, 115, 763

Chen, K.-J., Bromm, V., Heger, A., Jeon, M., & Woosley, S. 2015, ApJ, 802, 13

Chen, K.-J., Heger, A., Whalen, D. J., et al. 2017a, MNRAS, 467, 4731

Chen, K.-J., Heger, A., Woosley, S., Almgren, A., & Whalen, D. J. 2014, ApJ, 792, 44

Chen, K.-J., Moriya, T. J., Woosley, S., et al. 2017b, ApJ, 839, 85

Chen, K.-J., Whalen, D. J., Wollenberg, K. M. J., Glover, S. C. O., & Klessen, R. S. 2017c, *ApJ*, 844, 111

Chiaki, G., Susa, H., & Hirano, S. 2018, *MNRAS*, 475, 4378

Chiaki, G., & Tominaga, N. 2020, *MNRAS*, 498, 2676

Clark, P. C., Glover, S. C. O., Smith, R. J., et al. 2011, *Science*, 331, 1040

Corlies, L., Johnston, K. V., & Wise, J. H. 2018, *MNRAS*, 475, 4868

Couchman, H. M. P. 1991, *ApJL*, 368, L23

de Souza, R. S., Ishida, E. E. O., Johnson, J. L., Whalen, D. J., & Mesinger, A. 2013, *MNRAS*, 436, 1555

de Souza, R. S., Ishida, E. E. O., Whalen, D. J., Johnson, J. L., & Ferrara, A. 2014, *MNRAS*, 442, 1640

Dwarkadas, V. V. 2005, *ApJ*, 630, 892

Efstathiou, G., Davis, M., White, S. D. M., & Frenk, C. S. 1985, *ApJS*, 57, 241

Evans, Neal J., I., Dunham, M. M., Jørgensen, J. K., et al. 2009, *ApJS*, 181, 321

Frebel, A. 2010, *Astronomische Nachrichten*, 331, 474

Frebel, A., Aoki, W., Christlieb, N., et al. 2005, *Nature*, 434, 871

Gardner, J. P., Mather, J. C., Clampin, M., et al. 2006, *SSRv*, 123, 485

Glover, S. 2013, in *Astrophysics and Space Science Library*, Vol. 396, *Astrophysics and Space Science Library*, ed. T. Wiklind, B. Mobasher, & V. Bromm, 103

Glover, S. C. O., & Abel, T. 2008, *MNRAS*, 388, 1627

Glover, S. C. O., & Jappsen, A.-K. 2007, *ApJ*, 666, 1

Greif, T. H. 2015, *Computational Astrophysics and Cosmology*, 2, 3

Greif, T. H., Bromm, V., Clark, P. C., et al. 2012, *MNRAS*, 424, 399

Greif, T. H., Glover, S. C. O., Bromm, V., & Klessen, R. S. 2010, *ApJ*, 716, 510

Greif, T. H., Johnson, J. L., Bromm, V., & Klessen, R. S. 2007, *ApJ*, 670, 1

Greif, T. H., Johnson, J. L., Klessen, R. S., & Bromm, V. 2008, *MNRAS*, 387, 1021

Greif, T. H., Springel, V., White, S. D. M., et al. 2011, *ApJ*, 737, 75

Hartwig, T., Bromm, V., & Loeb, A. 2018a, *MNRAS*, 479, 2202

Hartwig, T., Ishigaki, M. N., Klessen, R. S., & Yoshida, N. 2019, *MNRAS*, 482, 1204

Hartwig, T., Yoshida, N., Magg, M., et al. 2018b, *MNRAS*, 478, 1795

Hasegawa, K., Umemura, M., & Susa, H. 2009, *MNRAS*, 445

Heger, A., & Woosley, S. E. 2002, *ApJ*, 567, 532

—. 2010, *ApJ*, 724, 341

Hirano, S., Hosokawa, T., Yoshida, N., & Kuiper, R. 2017, *Science*, 357, 1375

Hirano, S., Hosokawa, T., Yoshida, N., Omukai, K., & Yorke, H. W. 2015, *MNRAS*, 448, 568

Hirano, S., Hosokawa, T., Yoshida, N., et al. 2014, *ApJ*, 781, 60

Hosokawa, T., Omukai, K., Yoshida, N., & Yorke, H. W. 2011, *Science*, 334, 1250

Ishigaki, M. N., Tominaga, N., Kobayashi, C., & Nomoto, K. 2018, *ApJ*, 857, 46

Iwamoto, N., Umeda, H., Tominaga, N., Nomoto, K., & Maeda, K. 2005, *Science*, 309, 451

Jaura, O., Glover, S. C. O., Wollenberg, K. M. J., et al. 2022, *MNRAS*, 512, 116

Jeon, M., & Bromm, V. 2019, *MNRAS*, 485, 5939

Jeon, M., Pawlik, A. H., Bromm, V., & Milosavljević, M. 2014, *MNRAS*, 440, 3778

Jeon, M., Pawlik, A. H., Greif, T. H., et al. 2012, *ApJ*, 754, 34

Joggerst, C. C., Almgren, A., Bell, J., et al. 2010, *ApJ*, 709, 11

Joggerst, C. C., & Whalen, D. J. 2011, *ApJ*, 728, 129

Kalirai, J. 2018, *Contemporary Physics*, 59, 251

Karlsson, T., Johnson, J. L., & Bromm, V. 2008, *ApJ*, 679, 6

Kim, J.-G., Ostriker, E. C., & Filippova, N. 2021, *ApJ*, 911, 128

Kitayama, T., Yoshida, N., Susa, H., & Umemura, M. 2004, *ApJ*, 613, 631

Kroupa, P. 2001, *MNRAS*, 322, 231

Krumholz, M. R., McKee, C. F., & Bland-Hawthorn, J. 2019, *ARA&A*, 57, 227

Latif, M. A., Khochfar, S., Schleicher, D., & Whalen, D. J. 2021, *MNRAS*, 508, 1756

Latif, M. A., & Schleicher, D. 2020, *ApJL*, 902, L31

Latif, M. A., Whalen, D., & Khochfar, S. 2022, *ApJ*, 925, 28

Mackey, J., Bromm, V., & Hernquist, L. 2003, *ApJ*, 586, 1

Magg, M., Nordlander, T., Glover, S. C. O., et al. 2020, *MNRAS*, 498, 3703

McKee, C. F., Stacy, A., & Li, P. S. 2020, *MNRAS*, 496, 5528

McKee, C. F., & Tan, J. C. 2008, *ApJ*, 681, 771

Mesler, R. A., Whalen, D. J., Smidt, J., et al. 2014, *ApJ*, 787, 91

Moriya, T. J., Wong, K. C., Koyama, Y., et al. 2019, *PASJ*, 71, 59

Nakamura, F., & Umemura, M. 2001, *ApJ*, 548, 19

Navarro, J. F., Frenk, C. S., & White, S. D. M. 1996, *ApJ*, 462, 563

O’Shea, B. W., Wise, J. H., Xu, H., & Norman, M. L. 2015, *ApJL*, 807, L12

Ou, P.-S., Chen, K.-J., Chu, Y.-H., & Tsai, S.-H. 2023, *ApJ*, 944, 34

Paardekooper, J.-P., Khochfar, S., & Dalla Vecchia, C. 2015, *MNRAS*, 451, 2544

Patrick, S. J., Whalen, D. J., Latif, M. A., & Elford, J. S. 2023, *MNRAS*, 522, 3795

Pawlak, A. H., Milosavljević, M., & Bromm, V. 2013, *ApJ*, 767, 59

Paxton, B., Bildsten, L., Dotter, A., et al. 2011, *ApJS*, 192, 3

Paxton, B., Cantiello, M., Arras, P., et al. 2013, *ApJS*, 208, 4

Paxton, B., Marchant, P., Schwab, J., et al. 2015, *ApJS*, 220, 15

Paxton, B., Schwab, J., Bauer, E. B., et al. 2018, *ApJS*, 234, 34

Placco, V. M., Frebel, A., Beers, T. C., et al. 2016, *ApJ*, 833, 21

Riaz, R., Bovino, S., Vanaverbeke, S., & Schleicher, D. R. G. 2018, *MNRAS*, 479, 667

Ritter, J. S., Safranek-Shrader, C., Gnat, O., Milosavljević, M., & Bromm, V. 2012, *ApJ*, 761, 56

Ritter, J. S., Safranek-Shrader, C., Milosavljević, M., & Bromm, V. 2016, *MNRAS*, 463, 3354

Rydberg, C.-E., Whalen, D. J., Maturi, M., et al. 2020, *MNRAS*, 491, 2447

Safranek-Shrader, C., Milosavljević, M., & Bromm, V. 2014, *MNRAS*, 438, 1669

Salpeter, E. E. 1955, *ApJ*, 121, 161

Schaerer, D. 2002, *A&A*, 382, 28

Schneider, R., Omukai, K., Inoue, A. K., & Ferrara, A. 2006, *MNRAS*, 369, 1437

Sharda, P., Federrath, C., & Krumholz, M. R. 2020, *MNRAS*, 497, 336

Sluder, A., Ritter, J. S., Safranek-Shrader, C., Milosavljević, M., & Bromm, V. 2016, *MNRAS*, 456, 1410

Smidt, J., Whalen, D. J., Johnson, J. L., Surace, M., & Li, H. 2018, *ApJ*, 865, 126

Smidt, J., Whalen, D. J., Wiggins, B. K., et al. 2014, *ApJ*, 797, 97

Smith, B. D., & Sigurdsson, S. 2007, *ApJL*, 661, L5

Smith, B. D., Wise, J. H., O’Shea, B. W., Norman, M. L., & Khochfar, S. 2015, *MNRAS*, 452, 2822

Smith, N. 2014, *ARA&A*, 52, 487

Stacy, A., & Bromm, V. 2013, *MNRAS*, 433, 1094

Stacy, A., Greif, T. H., & Bromm, V. 2010, *MNRAS*, 403, 45

Stacy, A., McKee, C. F., Lee, A. T., Klein, R. I., & Li, P. S. 2022, *MNRAS*, 511, 5042

Susa, H. 2013, *ApJ*, 773, 185

—. 2019, *ApJ*, 877, 99

Susa, H., Hasegawa, K., & Tominaga, N. 2014, *ApJ*, 792, 32

Susa, H., & Umemura, M. 2006, *ApJL*, 645, L93

Susa, H., Umemura, M., & Hasegawa, K. 2009, *ApJ*, 702, 480

Tanaka, M., Moriya, T. J., & Yoshida, N. 2013, *MNRAS*, 435, 2483

Tanaka, M., Moriya, T. J., Yoshida, N., & Nomoto, K. 2012, *MNRAS*, 422, 2675

Tarumi, Y., Hartwig, T., & Magg, M. 2020, *ApJ*, 897, 58

Toro, E. F., Spruce, M., & Speares, W. 1994, *Shock Waves*, 4, 25

Turk, M. J., Abel, T., & O’Shea, B. 2009, *Science*, 325, 601

Umeda, H., & Nomoto, K. 2002, *ApJ*, 565, 385

Vink, J. S., de Koter, A., & Lamers, H. J. G. L. M. 2001, *A&A*, 369, 574

Whalen, D., Abel, T., & Norman, M. L. 2004, *ApJ*, 610, 14

Whalen, D., Hueckstaedt, R. M., & McConkie, T. O. 2010, *ApJ*, 712, 101

Whalen, D., O’Shea, B. W., Smidt, J., & Norman, M. L. 2008a, *ApJ*, 679, 925

Whalen, D., van Veelen, B., O’Shea, B. W., & Norman, M. L. 2008b, *ApJ*, 682, 49

Whalen, D. J. 2013, *Acta Polytechnica*, 53, 573

Whalen, D. J., & Fryer, C. L. 2012, *ApJL*, 756, L19

Whalen, D. J., Fryer, C. L., Holz, D. E., et al. 2013a, *ApJL*, 762, L6

Whalen, D. J., Joggerst, C. C., Fryer, C. L., et al. 2013b, *ApJ*, 768, 95

Whalen, D. J., Smidt, J., Johnson, J. L., et al. 2013c, *arXiv:1312.6330*

Whalen, D. J., Even, W., Frey, L. H., et al. 2013d, *ApJ*, 777, 110

Wise, J. H., & Abel, T. 2008a, *ApJ*, 684, 1

—. 2008b, *ApJ*, 685, 40

—. 2011, *MNRAS*, 414, 3458

Wise, J. H., Turk, M. J., Norman, M. L., & Abel, T. 2012, *ApJ*, 745, 50

Wollenberg, K. M. J., Glover, S. C. O., Clark, P. C., & Klessen, R. S. 2020, *MNRAS*, 494, 1871

Woodward, P., & Colella, P. 1984, *Journal of Computational Physics*, 54, 115

Xing, Q.-F., Zhao, G., Liu, Z.-W., et al. 2023, *Nature*, 618, 712

Yoshida, N., Omukai, K., & Hernquist, L. 2007, *ApJL*, 667, L117